Available online at www.sciencedirect.com
SCIENCE DIRECT®
ELSEVIER
Nuclear Instruments and Methods in Physics Research A 515 (2003) 575–588
NUCLEAR INSTRUMENTS & METHODS IN PHYSICS RESEARCH Section A
www.elsevier.com/locate/nima

# Texture analysis with the new HIPPO TOF diffractometer

H.-R. Wenk[a,*], L. Lutterotti[a], S. Vogel[b]

[a] Department of Earth and Planetary Science, University of California, Berkeley, CA 94720, USA
[b] Lujan Center, Los Alamos National Laboratory, MS H805, Los Alamos, NM 87545, USA

Received 14 April 2003; accepted 27 May 2003

**Abstract**

The new neutron time-of-flight (TOF) diffractometer HIPPO (High-Pressure-Preferred Orientation) at LANSCE (Los Alamos Neutron Science Center) is described and results for quantitative texture analysis of a standard sample are discussed. HIPPO overcomes the problem of weak neutron scattering intensities by taking advantage of the improved source at LANSCE, a short flight path (9 m) and a novel three-dimensional arrangement of detector banks with 1360 $^3$He tubes, on five conical rings with scattering angles ranging from $2\theta = 10^\circ$ to $150^\circ$. Flux at the sample is on the order of $10^7$ neutrons $cm^{-2}\,s^{-1}$. A large sample chamber (75 cm diameter well) can accommodate ancillary equipment such as an automatic sample changer/goniometer used in this study. This instrument was used to measure the texture of a round-robin limestone standard and extract orientation distribution data from TOF diffraction spectra with different methods (Rietveld harmonic method, Rietveld direct method, automatic fitting of individual peak intensities), and the results compare favorably. Also, there is good agreement with results obtained on the same sample measured at other facilities, but with greatly reduced measuring time for HIPPO.


*PACS:* 61.12.Ex; 81.40.Ef; 83.80.Nb

*Keywords:* Neutron diffraction; Texture analysis; Rietveld

## 1. Introduction

In 1997, as part of the Spallation Source Upgrade project, the University of California Materials Research Diffractometer, proposed by a consortium of UC faculty and National Laboratory researchers was chosen as one of the three new diffractometers to be built at the Los Alamos Neutron Science Center (LANSCE) [1]. This diffractometer, more recently known as HIPPO (for High-Pressure-Preferred Orientation, two of its main functions) started a user program in summer 2002 and in this paper we are presenting first results of quantitative texture analysis, together with a description of the unique features of this instrument and streamlined procedures of data analysis.

The diffractometer was built to attract mainstream chemists, materials and earth scientists to neutron diffraction to take advantage of outstanding features of neutrons for materials analysis that cannot be achieved with conventional and

*Corresponding author. Tel.: +510-642-7431; fax: +510-643-9980.
*E-mail address:* wenk@seismo.berkeley.edu (H.-R. Wenk).

0168-9002/$ - see front matter © 2003 Elsevier B.V. All rights reserved.
doi:10.1016/j.nima.2003.05.001

synchrotron X-rays. Among the primary advantages of neutrons is their low attenuation by most elements that makes it possible to study large sample volumes (1 $mm^3$ to several $cm^3$) that are representative of the bulk properties, compared to the surface sensitivity of X-rays or electrons. It also enables the construction of environmental cells to investigate samples under conditions of high and low temperature, pressure, stress or magnetic and electric fields. Parallel with the low attenuation goes the weak interaction of neutrons and matter, compared to electrons and X-rays, and thus normally long counting times are required. The aim to obtain high count rate was a prime consideration in the design of HIPPO in order to be able to investigate time-dependent processes, as well as representative sample series, for instance of varying chemical composition or deformation history.

Preferred orientation (or texture) is one of the characteristic features of many polycrystalline materials and, combined with the single crystal anisotropy, the main cause of anisotropic physical properties of bulk solids. Neutron diffraction was first applied by Brockhouse [2] to study textures in magnetic nickel but only in the 1980s, with the wider availability of neutron sources, did it become a viable method and presently several beamlines in different facilities are used routinely for texture analysis. A conventional neutron texture experiment employs monochromatic radiation. The detector is set at the Bragg angle $2\theta$ for a selected set of lattice planes $h\ k\ l$. The pole densities corresponding to this set of lattice planes in different sample directions are obtained by rotating the sample around two goniometer axes, to cover the entire orientation range and several pole figures are measured consecutively. This method is analogous to the X-ray pole figure goniometer method.

It is also possible to use *position-sensitive detectors*, which simultaneously record intensities resulting from diffraction of monochromatic radiation along a ring (1-D), or over an area (2-D), rather than at a point. In the case of 1-D position-sensitive detectors, the ring can be mounted on a diffractometer so that it covers the whole 90° range of goniometer coordinate $\chi$ [3] or that it records a continuous $2\theta$ range [4,5].

Another method to measure a spectrum simultaneously is at a fixed detector position but with *polychromatic* neutrons and a detector system that can measure the time of flight (TOF) of neutrons and discriminate their energies [6,7]. In this case a detector, fixed at a scattering angle, records a whole spectrum with many Bragg peaks. Position-sensitive detectors and TOF have been combined [8]. With a 2-D position-sensitive detector, as it is available at IPNS (Intense Pulsed Neutron Source at Argonne National Laboratory) and LANSCE, a whole pole figure range can be recorded simultaneously [9]. A disadvantage of this technique is cumbersome data extraction due to geometric distortions and numerous non-linear corrections. Therefore, point detectors are preferred, but instead of a single detector, several detectors can be used simultaneously. This concept has first been introduced at the pulsed neutron source in Dubna, where the NSHR diffractometer uses seven detectors at different diffraction angles in the same plane [10] and the newer SKAT diffractometer uses 24 detector tubes, 60 mm in diameter, arranged on a ring at a fixed diffraction angle ($2\theta = 90°$) [11]. With such multidetector systems fewer sample rotations are necessary to cover the pole figure. The Dubna system was the basis for the design of HIPPO, except that detector coverage was greatly increased, with not only one, but five rings of detector panels at constant $2\theta$ and up to 384 tubes of 12 mm diameter in a ring.

The reliability of neutron pole figure measurements was highlighted by excellent results of a round-robin experiment in which over 15 facilities participated [10,12,13] and, if it were more available, neutron diffraction would clearly be the method of choice for bulk texture measurements. The round-robin experiment documented that pole figure measurements with neutron diffraction of the same sample by different laboratories are much more reproducible than those with conventional X-ray diffraction, mainly because of better statistics and absence of instrument-dependent defocusing and absorption corrections. In this report, we will use this same standard round-robin sample, an experimentally deformed limestone, with HIPPO and illustrate that satisfactory results can be obtained both with

individual peak analysis and fitting of spectra with the Rietveld method. In general, neutron diffraction texture measurements have the advantage that they can be performed on coarse-grained samples and still provide good grain statistics [14], are easily extendable to non-ambient conditions [15] and provide information about magnetic as well as crystallographic orientation in polycrystals [16].

## 2. Instrument characteristics

In designing a diffractometer, a balance must be made between intensity (decreasing approximately with $1/L^2$, where $L$ is the flight path length) and resolution (increasing approximately with $1/L$). The goal for HIPPO was to have the highest count rates available at the cost of only moderate resolution, which was achieved by an instrument design consisting of detectors covering a large surface, and a short flight path. In HIPPO, the sample is at a 9 m distance from the moderator which consists of a decoupled high-intensity/low-resolution water moderator of 2.5 cm thickness with a square surface of $13 \times 13\,\mathrm{cm}^2$. The time-averaged flux on a sample, with the proton accelerator operating at 120 μA, is $\sim 2.4 \times 10^7$ neutrons $\mathrm{cm}^{-2}\,\mathrm{s}^{-1}$ for neutron energies in the "thermal" ($<0.4$ eV) range suitable for diffraction work.

The usable range of the TOF frames on HIPPO's 9 m flight path covers 0.5–24 ms. Beyond 24 ms, the incident intensity from the moderator is so low that no usable data can be obtained. Therefore, for a 20 Hz operation, which gives a 50 ms frame, there is no "frame overlap" effect with a Bragg reflection from a previous TOF frame appearing as a background feature.

To maintain resolution characteristics that are independent of detector azimuthal angle, the collimation system views a circular portion of the moderator surface 12 cm in diameter and produces a circular beam with a maximum diameter of 2 cm at the sample position. Additional "shadow shield" collimators can be positioned closer to the sample as needed to reduce the penumbra scattering. Collimator inserts fitted after the last collimating element can be used to produce beams down to 5 mm diameter as needed. Beyond the sample position is a beam stop.

1360 $^3$He detector tubes are arranged in 50 panels on five rings (banks) surrounding the incident beam (Fig. 1). The detector layout comprises five angular ranges covering both low and high angles and characteristics of each range are listed in Table 1. The $d$-spacing is determined from the chosen TOF frame of 0.5–24 ms. The detector panels are tilted relative to the scattered neutron paths to give a more constant resolution across their surfaces. The tilt compensates for the change in $2\theta$ due to the finite angular range covered by each panel with a corresponding change in the sample-to-detector flight path. The total detector coverage is $4.74\,\mathrm{m}^2$, compared with a detector area for HIPPO's predecessor HIPD (High-Intensity Powder Diffractometer) at LANSCE of $0.44\,\mathrm{m}^2$. Detector panels are composed of sets of 10 atm $^3$He detector tubes with lengths ranging from 46 cm for the backscattering angle to 15 cm for the most forward scattering angle.

The large sample chamber is built to accommodate a variety of ancillary equipment. It has an opening 60 cm above the neutron beam centerline with a "standard" diameter of 75 cm, allowing interchange of ancillary equipment with other LANSCE beamlines. The walls of this chamber are 6.3 mm aluminum to minimize attenuation of scattered neutrons while maintaining structural stability. The 90° panels view the sample through 1.5-mm-thick aluminum windows. For most experiments, the chamber is not evacuated during the course of an experiment. A range of ancillary equipment is available for HIPPO and we just mention cryogenic equipment (displex system capable of ca. 10–300 K), high temperature vacuum furnaces (300–1500 K), a torroidal anvil high-pressure cell (30 GPa and 2000 K), a multi-position sample changer, a kappa geometry 3-circle goniometer and a load frame. Only the automated sample changer was used for this experiment (Fig. 2).

Data acquisition details for HIPPO are outlined in Table 2. The width of each TOF bin, $\Delta T$, is chosen such that $\Delta T/T$ is equal to the TOF bin factor. These are chosen for each detector to give

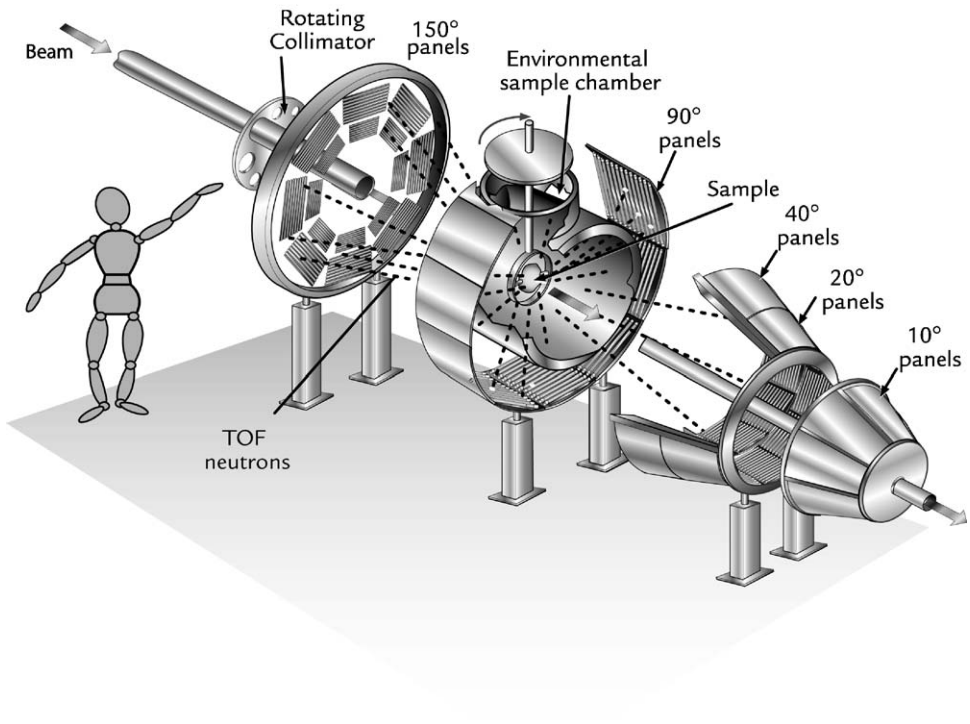


Fig. 1. Schematic view of the HIPPO diffractometer with five banks of detector panels arranged on rings. For scale a sketch of a fairly large person is added. The distance from the 150° panels to the 10° panels is 3 m.

Table 1
Detector specifications for HIPPO

| Nominal angle | No. panels | No. tubes | Area ($m^2$) | $d$ Range (Å) | Resolution (%) |
|---|---|---|---|---|---|
| $2\theta = 150°$ | 8 | 192 | 1.08 | 0.12–4.80 | 0.37 |
| 90° | 10 | 240 | 1.08 | 0.17–6.90 | 0.74 |
| 40° | 12 | 288 | 1.08 | 0.35–13.9 | 1.8 |
| 20° | 12 | 384 | 0.96 | 0.65–26.1 | 4.6 |
| 10° | 8 | 256 | 0.54 | 1.19–47.5 | 9.2 |
| Total | 50 | 1360 | 4.74 | | |

The $d$ ranges are for 0.5–9 Å wavelength range and the resolution $\Delta T/T = \Delta d/d$ is full-width at half-maximum over position.

approximately 10 TOF bins across the nominal resolution width anticipated at each scattering angle and about 30 TOF bins across the base of the peak. However, most experiments on HIPPO do not use all detectors; for example, texture measurements as described here only use $2\theta = 150°$, 90° and 40° banks because of the low resolution of low-angle detectors.

### 2.1. Data acquisition system (DAQ)

The DAQ uses commercial VXI crates controlled by VME Power PC single-board processors. Each VXI crate hosts up to eight TOF modules; each module can service up to 16 detector tubes. The system has 13 VXI crates; two each for the 150° and 10° detector banks, and three for the $2\theta = 20°$, 40° and 90° detector banks. Data are transferred from the DAQ to a data processing and display PC over a 100 Mbit/s network. Total save time between runs is currently 30 s, but will further decrease in the future, as required for instance for kinetics studies.

The user controls the instrument through the Graphical User Interface (GUI) or Perl scripts that provide access to the system to allow initiation of

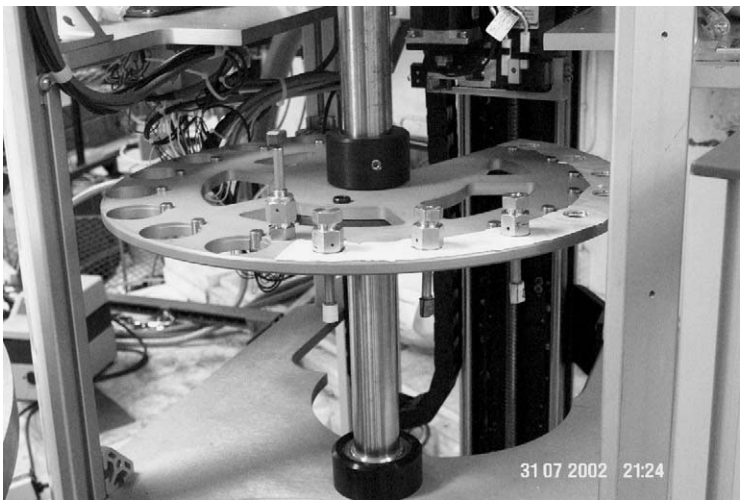


Fig. 2. The automatic sample changer that can accommodate 32 texture samples (or 100 powder samples). In the image shown, texture samples are mounted on vanadium rods.

Table 2
Data acquisition details for HIPPO

| Nominal angle | TOF bin factor | No. tubes | TOF ch./tube | Total TOF ch. |
|---|---|---|---|---|
| $2\theta = 150^\circ$ | 0.0004 | 192 | 10,344 | 1,986,048 |
| $90^\circ$ | 0.0008 | 240 | 5001 | 1,200,240 |
| $40^\circ$ | 0.0012 | 288 | 3298 | 949,824 |
| $20^\circ$ | 0.0016 | 384 | 2461 | 945,024 |
| $10^\circ$ | 0.0032 | 256 | 1222 | 312,832 |
| Total | | 1360 | | 5,393,968 |

data collection, display of spectra, control of special environment equipment, etc. Due to the short count times possible with HIPPO, automation of DAQ and sample changes, orientation changes, or changes of sample environment parameters like temperature was implemented. The detector systems are attached to the real-time portion, which captures the data in digital form and generates the TOF histograms. The data of a finished histogram are then transferred from the TOF module to the PC server that creates the Nexus/Hierarchical Data File (HDF, http://www.neutron.anl.gov/nexus) for archival. These HDF files contain data for all individual detector tubes and are over 20 MB in size. Generally, they are of little interest to the end user. The raw data are, therefore, binned for each detector panel or, if orientation information is not important, for all detector panels of a bank. This requires accurate calibration to determine the exact position of each detector tube and the corresponding flight path. Also, for texture experiments it is necessary to determine the detector efficiency. Both can be achieved with a powder standard with precisely known lattice parameters and a similar geometry as the actual sample. This standard ($CaF_2$ is commonly used) must be measured periodically to ascertain that the alignment of the instrument and electronic components has not changed and also to determine if all individual detector tubes are working to specifications. With the calibration file the raw data are then binned into a compact ASCII file in GSAS format (GDA, GSAS format [17]) that is provided to the user for further analysis. Fig. 3 displays portions of all spectra from the limestone sample for $2\theta = 150^\circ$, $90^\circ$ and $40^\circ$ detectors for one sample rotation position. As is immediately obvious, the resolution decreases with decreasing diffraction angle. Within one bank relative intensities of a given diffraction peak vary from detector to detector. This is an indication that the sample displays preferred orientation and the intensity differences are used to extract quantitative texture information as will be described in the next section.

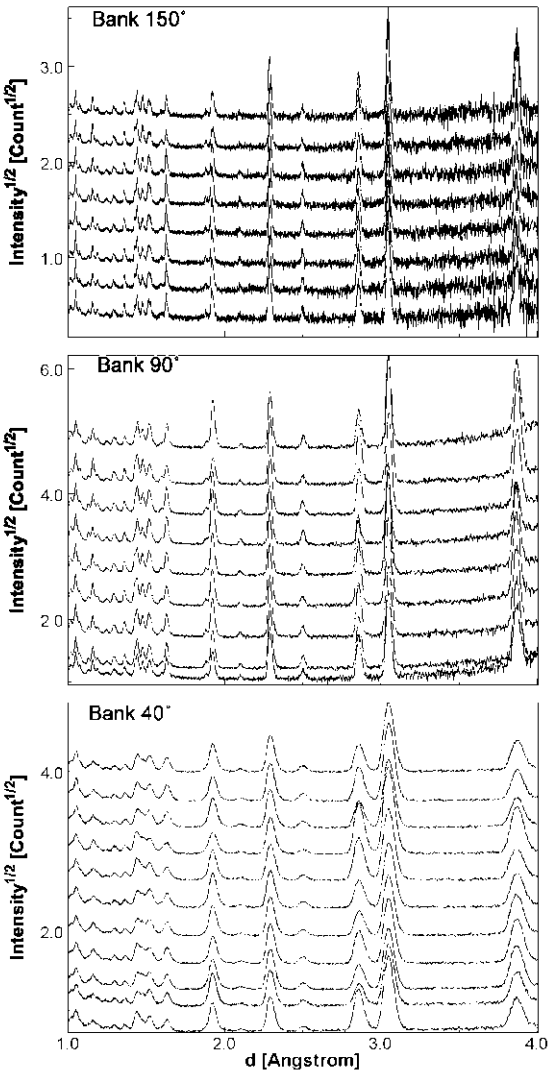


Fig. 3. Diffraction spectra for limestone recorded by detectors on banks $2\theta = 150°$, $90°$ and $40°$ for one rotation setting. Relative intensity variations illustrate presence of texture. Some spectra are more closely spaced due to variations in detector sensitivity. Resolution decreases with diffraction angle.

## 3. Texture analysis of limestone

### 3.1. Experimental

The goal of this work is to quantitatively establish the texture measurement capabilities of HIPPO. This is best done by using a standard sample with a well-known texture. We chose to use the experimentally deformed limestone that served as a round robin [12]. The cube (approximately $1\,cm^3$) with rounded corners was mounted on a thin Al rod shielded with a Cd foil for minimal diffraction interference and inserted into the automatic sample changer (Fig. 2). The sample changer enables unattended automated processing of up to 32 texture samples or up to 100 powder samples, without a need to open the sample chamber or close the shutter. In the sample changer, a sample in the tray is rotated into position, then grabbed by an arm on a goniometer with two rotations centered on the incident beam (only one was used in this study). Spectra were recorded for 15 min of beam time. No incident beam monitor was available during this run cycle and due to slight variations in proton current the neutron flux was not constant, requiring additional corrections during the texture refinement. The sample was rotated in eight 22.5° increments about the vertical axis (i.e. the axis of the sample chamber and perpendicular to the incident beam). The sample was measured twice, in September 2002 with 30 detector panels and in January 2003 with 28 detector panels (two were defective at that time). We will mainly use the newer data set.

Raw data were binned as described above and output in GSAS format that served as data for the texture analysis. Data from 30 panels ($2\theta = 150°$, $90°$ and $40°$ banks) and eight rotations provided a total of $8 \times 30 = 240$ spectra (224 for the second measurement). The raw spectra, normalized by the average incident spectrum, for the $2\theta = 40°$ bank are shown in Fig. 4 (bottom) ordered first according to rotation increments (eight) and each set stacked according to detector panels (12). This figure is from the first set of measurements, because it illustrates better some of the complexities that arise with a multidetector diffractometer such as HIPPO and requires rather sophisticated data processing.

Diffraction peaks are clearly visible as vertical lines, but the lines shift slightly both as function of rotation for a single detector and for the same rotation but among different detectors. The first shifts are due to the fact that the sample precesses (i.e. the rotation axis does not coincide with the

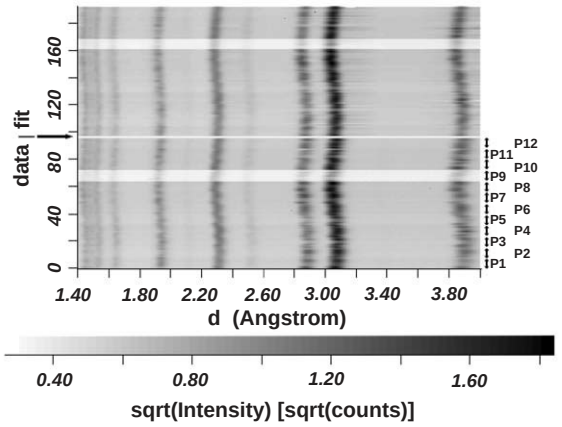


Fig. 4. Plot of diffraction spectra for $2\theta = 40^\circ$ bank for the first set of measurements. Twelve panels in a stack representation for eight rotations (arrows mark panes). Peak shifts and variations in background intensity indicate problems with sample alignment and instrument calibration. Bottom: Measured spectra (corrected for incident beam spectrum); top: spectra after Rietveld fit. Dark colors are high intensities.

sample axis), mostly due to misalignment of the sample on the holder. (In the second set of measurements this sample alignment problem was improved.) The second and more significant oscillation (shifts in *d*-spacings among panels) stems from the fact that the flight path for the various detectors was not the same as during the calibration, due to sample misalignment. This is particularly critical for low-angle detectors ($2\theta = 40^\circ$) with tubes highly inclined to the beam. There are also clear variations in background intensity (and corresponding peak intensities), both as function of rotation and detector. The first intensity variation suggests that the sample rotates in and out of the beam center, or that the incident beam intensity varies in the course of the experiment due to variations in proton current. The second variation is due to differences in detector efficiencies. For example, detector panel 9 has much lower count rates than the other detector panels on the $40^\circ$ bank. All these factors need to be considered in the data processing and proper corrections need to be introduced. (Note that the positional corrections are required not only for texture experiments but also for all diffraction experiments with HIPPO.)

Texture analysis takes advantage of the HIPPO feature that many detectors are available and each detector records intensities from differently oriented crystals according to Bragg's law that requires that lattice planes are in reflection position for incident and diffracted neutron beam. The orientation of lattice plane normals that are measured with individual detectors is best shown in a pole figure representation and Fig. 5a illustrates the coverage with the 30 detectors relative to incident beam (X) and axis of sample chamber (center). If the sample is rotated in eight increments of $22.5^\circ$ about the vertical axis the coverage is greatly improved (Fig. 5b). Note that the coverage is best near the periphery. Only the low-resolution $2\theta = 40^\circ$ detectors contribute to the coverage near the center of the pole figure. In these plots, angular locations of the detector panels are shown with small symbols, representative of the center of the detector panel. In reality, each location extends over a larger area determined by the size of the panels which limits the angular resolution (10–20°).

There are various ways to extract texture information from diffraction spectra. We will show two basic methods and compare results. The first method is to use the Rietveld method [18] of whole spectra fitting by refining instrumental, structural and textural parameters from all 240 spectra simultaneously. The second method is the more conventional approach to extract peak intensities for some diffraction peaks directly from the spectrum. This method is necessary if spectra contain interferences, e.g. diffractions from ancillary equipment such as furnaces.

### 3.2. Data analysis using the Rietveld method

The first approach relies on the Rietveld method to fit whole TOF spectra. There are presently two software packages that enable texture determinations with the Rietveld method. GSAS [13] uses a direct refinement of parameters with a diagonal matrix approach. The program offers many options for crystal structure determination/refinements but for texture it is restricted to the harmonic method. Because derivatives for the least-squares optimization are computed

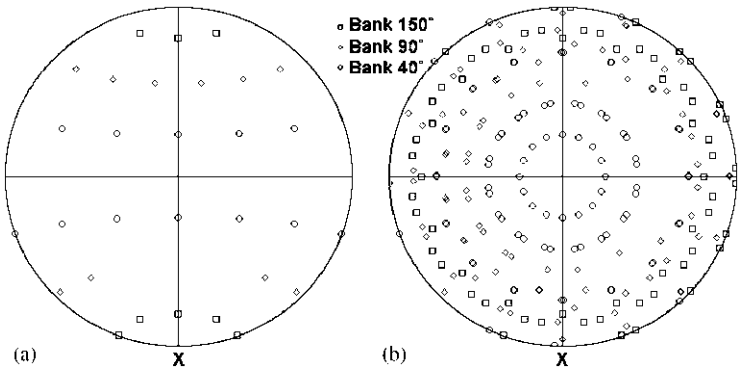


Fig. 5. Pole figure coverage with 30 detectors for $2\theta = 150°$, $90°$ and $40°$ banks (different symbols). Sample chamber axis is in the center. Incident neutron beam is at $X$. (a) Coverage with single setting. (b) Coverage with eight $22.5°$ sample rotations as used in this study.

analytically it is relatively fast. MAUD [19] uses a Marquardt least-squares fit approach with a numerical derivative computation. The latter provides more flexibility for incorporating different models in the refinement, but the refinement is slower than with GSAS. The gap in speed has been reduced by reducing redundant computation through object-oriented techniques. For texture studies, MAUD has the advantage that different algorithms, even non-analytical ones, can be used to obtain the orientation distribution function (ODF) in Fourier space (harmonic method), as well as in direct space (e.g. WIMV and maximum entropy). In a previous contribution, we have verified that for the harmonic method and identical constraints GSAS and MAUD produce similar texture results [20]. Here we use MAUD exclusively, in part because the present version of GSAS cannot analyze more than 99 spectra simultaneously.

Initial data are spectra as those shown in Fig. 3 but for eight sample rotations. A $d$-range from 1.0 to 4.0 Å was selected. Instrumental parameters, background function, microstructural features (relative isotropic crystallite size and r.m.s. microstrain), crystallographic parameters (lattice parameters, atomic positions) and texture were refined. Instrumental uncertainties for HIPPO required us to refine several correction functions as well. Two correction functions are related to the sample: a sample position (causing peak shifts) and a sample scale factor (because the sample was potentially not in all rotations in the center of the beam and because of changes in proton flux). Eight sample correction parameters were refined for each rotation increment. (For the second set of measurements the sample precession and position errors refined nearly to zero and were then successively excluded from the optimization procedure.) Two correction functions are used to account for detector uncertainties. A detector scale factor was refined to correct for detector efficiency, but assuming that the characteristics did not change in the course of the experiment. A separate offset parameter for each detector was refined to adjust for sample misalignment. Thirty (28 for the second experiment) detector correction parameters were refined for each. We did not refine an individual scale factor for each spectrum, as is done in GSAS, because such scale factors are highly correlated with texture and influence the solution. The correlation coefficients between scale factors and texture coefficients (in the harmonic method) are on the average three times higher if all individual scale factors are refined, than refining a single scale factor for each panel and rotation increment (the maximum correlation coefficient is about 6 times higher). The results obtained from the first measurement were in good agreement with those of the second, after applying all the corrections, and we will just present the results for the second measurement.

The refinement proceeded in cycles on 224 spectra simultaneously. First instrument and

background parameters were refined (54 and 18, respectively). In a second step, crystallographic parameters were added to the refinement (cell parameters, one isotropic B factor and fractional coordinate $x$ for the oxygen) and subsequently peak profile parameters and sample displacement errors for a total of 82 parameters. Finally, texture parameters were added also. For texture, the harmonic method and direct methods were used. In the case of direct methods, the newly developed version of WIMV that allows data to be entered at arbitrary positions (rather than the conventional $5^\circ \times 5^\circ$ grid), called EWIMV was employed. Fig. 6 shows one spectrum from a $2\theta = 150^\circ$ detector and the fitted curve for EWIMV. The computer used was an Apple Powerbook G4/800 MHz with 1 GB of RAM. The computation time for the last cycle of three iterations (sufficient to ensure convergence of the solution), including the texture parameters, was of about 1.5 h for the harmonic method (with a memory requirement of about 700 MB) and 55 min for the EWIMV algorithm (with a memory requirement of about 300 MB).

In the case of the harmonic refinement, the expansion was carried to a maximum order $L_{max} = 8$ (113 coefficients for trigonal crystal and triclinic sample symmetry). The memory requirement for the Marquardt least-squares refinement is at least equal to the number of refined parameters times the number of data points. For $L_{max} = 8$, the total number of parameters is 195 and the 224 spectra add to a total of 458 915 data points (the number of data depend on detector bank and selected $d$-range). Thus, the calculation requires more than 700 MB for double precision floating point arithmetic. $L > 8$ would require more than 1 GB of memory, exceeding the limit of our computer. From the ODF, some pole figures were recalculated and results for the harmonic method are shown in Fig. 7a. The initial sample orientation was arbitrary and pole figures are therefore oblique, when compared with those reported previously [12].

The EWIMV algorithm was derived from the WIMV method [21] to provide a better integration between the Rietveld method and the texture computation. The main differences of EWIMV relative to WIMV are: (a) the ODF cell path for each individual measurement and reflection is computed explicitly for the true measurement angles, no longer requiring a regular grid coverage and interpolation, (b) the tube cell projection of the paths, in analogy to the ADC (Arbitrarily Defined Cells) method [22,23], improves the smoothness of the ODF, (c) a modified iteration algorithm based on an entropy principle increases

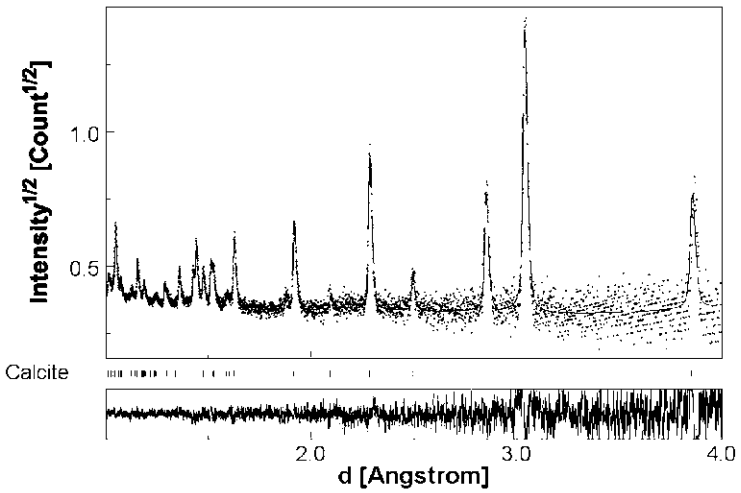


Fig. 6. Spectrum, normalized for incident beam, from a detector panel of the $2\theta = 150^\circ$ bank with recorded data (dots) and fit (line) using the MAUD Rietveld method with EWIMV.

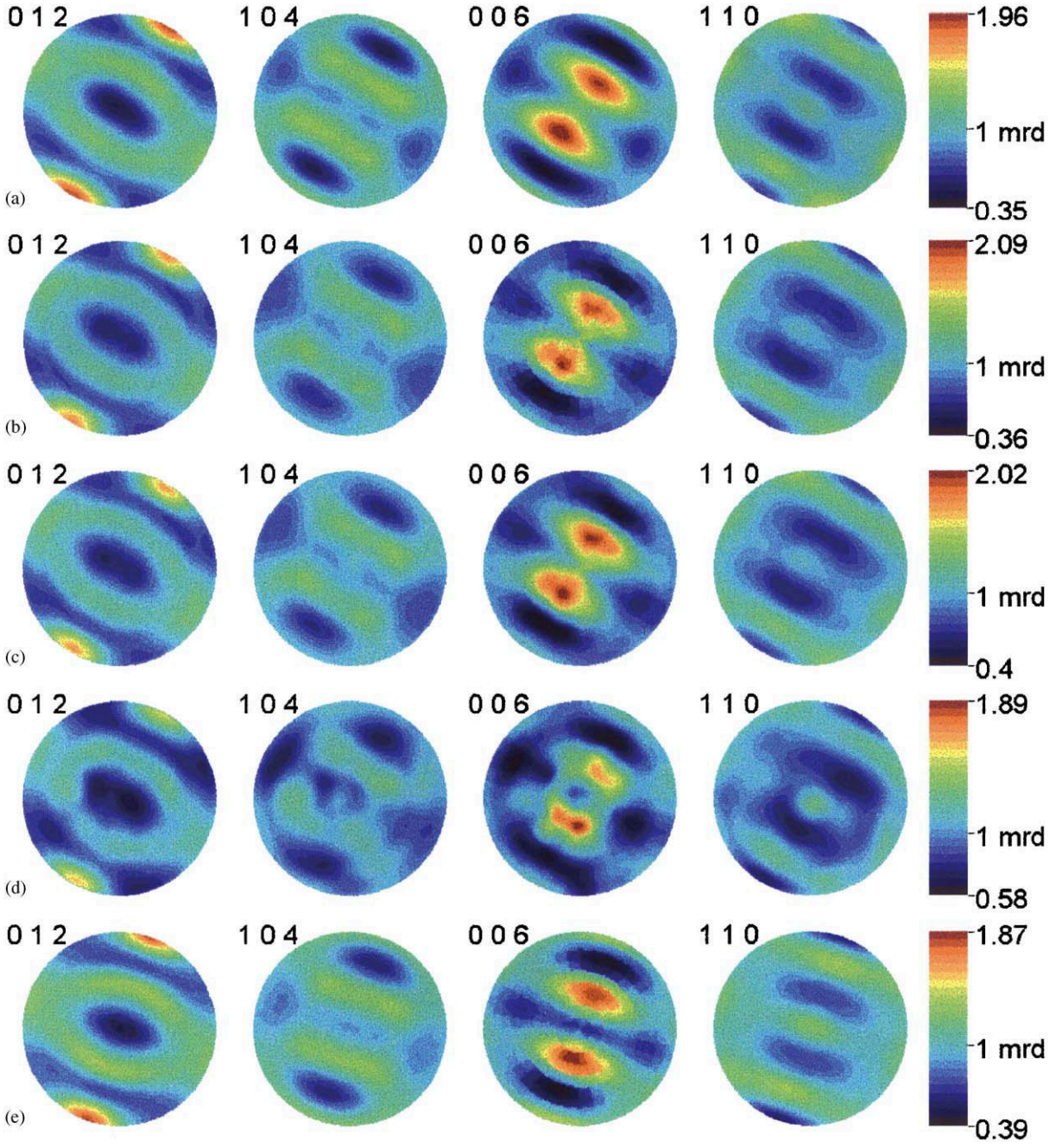


Fig. 7. Pole figures for standard sample of experimentally deformed limestone calculated from the ODF. Equal area projection, linear contours (in multiples of a random distribution). (a) Rietveld refinement with harmonic method, expansion to $L_{max} = 8$. (b) Rietveld refinement with the EWIMV method. (c) Same as (b) but graphically smoothed with a Gauss filter. (d) Individual peak extraction method, with ODF calculated from five incomplete pole figures such as that in Fig. 8b. (e) Comparative results for the EWIMV method for data obtained on the instrument D20 at ILL.

Table 3
Lattice parameters and atomic coordinate $x$ of oxygen and temperature factor B refined from the limestone standard specimen with MAUD

| | $a$ (Å) | $c$ (Å) | $x_O$ | $B$ |
|---|---|---|---|---|
| HIPPO harmonic | 4.9815(1) | 17.0837(2) | 0.2556(1) | 0.706(2) |
| HIPPO EWIMV | 4.9816(1) | 17.0838(2) | 0.2557(1) | 0.706(2) |
| ILL-D20 | 4.98129(3) | 17.0764(2) | 0.2558(1) | 0.800(7) |
| IPNS-GPPD [19] | 4.9824(1) | 17.0774(4) | 0.2556(1) | |

speed and convergence, (d) different cell sizes can be selected. In the present implementation only cell sizes that, if multiplied by an integer ($>1$) result in 30°, can be used. For the analysis of limestone, the best results in terms of ODF coverage and smoothness were obtained for a cell size of 10° and the default tube projection distance equal to 2 times the cell size. The convergence of the solution was obtained always after 10 iterations. Texture results for EWIMV are shown in Fig. 7b. In the EWIMV pole figures the individual cell pattern is visible, particularly for the 006 pole figure. It is useful to assess the quality of the data, e.g. by ascertaining that there are no large deviations between individual cells or sporadic values. By graphical smoothing of the pole figure pixel values with a Gauss filter, the cell boundaries disappear and we obtain a smoother visual effect, without changing minima and maxima significantly and this pattern is similar to the results of the harmonic method (Fig. 7c).

For comparison, the same analysis with EWIMV was performed on a data set measured on the same sample with the new D20 diffractometer at ILL (Institut Laue Langevin) [24]. For D20 monochromatic neutrons are used ($\lambda = 1.290713$ Å) and a 1-D position-sensitive detector collects data over an angular range of 120°. The coverage was assured by a regular mesh in $\chi$ and $\phi$ of $10° \times 10°$ and two $\omega$ positions (50° and 125°). Only the peripheral part of the pole figure was measured (90–60°). Recalculated pole figures are shown in Fig. 7e.

Results for crystallographic parameters are shown in Table 3. They illustrate that lattice parameters as well as atomic positions ($x$ for oxygen and temperature factor B) for both approaches compare favorably and also agree with values obtained earlier with the IPNS GPPD diffractometer [19]. The calculated standard deviation for lattice parameters may not represent the true error. For TOF data, lattice parameters are very sensitive to instrument calibration and sample positioning and, for monochromatic neutrons, to the exact wavelength produced by the monochromator.

For the first set of measurements, corresponding to Fig. 4, the rotation center displacement in the plane normal to the incident beam refined to –2.26(1) and –2.46(1) mm in two orthogonal directions. This displacement is the cause for the sinusoidal variation of peak position with detector panel. A sample precession error radius of 0.963(4) mm and arbitrary starting angle of 24.0(2)° determines the peak shift with rotation.

For the second set of measurements the correction parameters refined as follows. No displacement of the rotation center was found and the precession-dependent correction parameter for position refined to a value of 0.002(3) mm, i.e. the sample precessed on a circle of this radius around the diffraction center. The rotation-dependent intensity scaling parameter refined to values ranging from 0.902(1) to 1.205(1). The detector correction parameters for position (the DIFC parameter in GSAS that converts TOF to $d$-spacings) refined to a unique value for the 150° and 90° banks, but to values ranging from 1941.35(9) to 1981.58(9) Å/μs for panels of the 40° bank. We mentioned earlier that we associate this with the different geometry of the texture sample and the calibration standard, which is particularly sensitive for low-angle detectors. The detector scale parameter refined to values ranging from 0.993(1) to 1.69(1) for panels of the 150° bank, from 0.466(1) to 1.428(3) for the 90° bank, and from 0.620(1) to 1.35(1) for the 40° bank. Note that there are large variations for scale parameters of panels within one bank.

### 3.3. Texture extraction using individual peak intensities

Using the Matlab software environment a program was written to extract integrated intensities

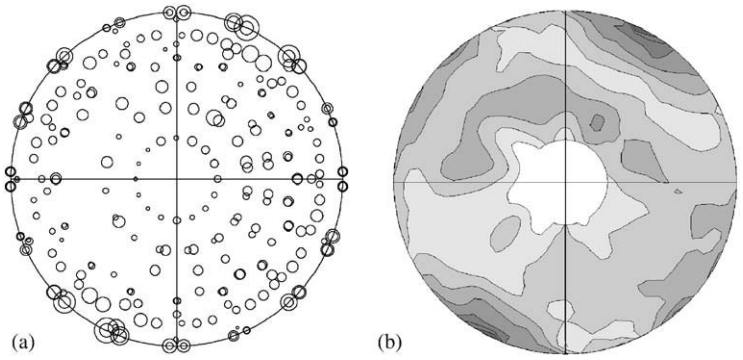


Fig. 8. Pole figure determination with individual peak intensity extraction method: (a) coverage of pole figure with data. Circle size is proportional to intensities of (0 1 2); (b) interpolated and contoured (0 1 2) pole figure that is used to calculate the ODF.

of diffraction peaks from TOF spectra. A pseudo-Voigt peak shape is assumed and positions of one or several (in our case five) peaks are selected on one spectrum. The program then fits the pseudo-Voigt function to the peak by adjusting position and intensity and subtracting background. This is done automatically in the whole series of 240 spectra. These data need to be corrected for factors discussed with Fig. 4. Peak shifts due to misalignment are taken into account by position refinement. Peak intensities are first normalized by the absolute TOF intensity spectrum of the incident neutron beam specific to each detector panel which was obtained by measuring incoherent scattering from a vanadium sample and accounts for systematic efficiency variations between individual detector panels of a bank, and corrected by a $\theta$-dependent Lorentz factor. These corrected integrated intensities were then entered into the pole figure as shown for 0 1 2 in Fig. 8a, with circle size proportional to the intensity. By triangular interpolation values for the standard $5^\circ \times 5^\circ$ pole figure grid were obtained (a contoured pole figure is shown in Fig. 8b). This pole figure is incomplete and the center is not covered. From five incomplete pole figures ($\chi = 90^\circ$ to $50^\circ$)—012, 104, 006, 110 and 113—an orientation distribution function (ODF) was calculated with the WIMV method as implemented in the software BEARTEX [25] and normalized complete pole figures were recalculated (Fig. 7d).

## 4. Discussion

With the successful texture analysis of the standard sample of limestone we have demonstrated that the new HIPPO diffractometer at LANSCE is capable of measuring textures quantitatively. A glance at Fig. 7 (and also comparing HIPPO results with those measured on other diffractometers [9,10,12,13,19] documents that textures from HIPPO are very similar, both in pattern and pole densities, with those from other facilities measuring the same sample. This is also confirmed in Table 4 that gives values for the texture index F2 [26] and maximum and minimum of the ODF. A considerable difference is the time required for data collection. For HIPPO, one sample with eight rotation increments was measured in 2 h, compared to the D20 where measurements took around 20 h, and at Dubna the texture measurement of a sample takes well over a day. With HIPPO's automatic sample changer textures on sample series of over 10/day can be measured without operator intervention.

It was also reassuring to see that different methods of texture analysis provide similar results but a brief discussion of differences and advantages of each method is appropriate. If well-separated individual peaks exist, the peak extraction method is fast, easy to use and does not require much computing power. However, in the presence of significant instrumental uncertainties affecting the measured peak intensities, as in the

Table 4
Texture index and minimum and maximum values for the ODF as obtained by the different procedures

| Analysis | Texture index | Minimum (m.r.d.) | Maximum (m.r.d.) |
|---|---|---|---|
| Hippo-harmonic | 1.226 | –0.053 | 2.896 |
| Hippo-EWIMV | 1.301 | 0.188 | 4.79 |
| Hippo-individual intensities | 1.251 | 0.171 | 4.70 |
| ILL-D20-EWIMV | 1.308 | 0.247 | 3.34 |

present work (see discussion of Fig. 4) the Rietveld method will generally provide more accurate texture information because experimental uncertainties are constrained by a physical model. The individual peak method must be applied if spurious parasitic peaks (e.g. from ancillary instruments such as furnace metal [27]) preclude the use of the Rietveld method.

Texture analysis with the Rietveld method is now well established. The harmonic method and direct methods produce similar results for weak texture, though the ODF maximum and minimum is smaller, when computed with the harmonic method. Because of the smoothing effect of harmonic functions, the harmonic pole figures may have a more pleasing appearance than the EWIMV pole figures where discrete cells are visible. But a word of caution is appropriate. Expansion to order 8 does not provide a very high resolution (in the range of 45°) and most X-ray texture analyses use expansions to order $L_{max} = 24$ or higher. The weak texture of the limestone standard is reasonably expressed with low- order harmonic functions but for sharper textures the method may be problematic. Xie et al. [20] illustrated that irregular coverage, combined with variable detector efficiencies and absorption effects produces serious artifacts. Also the problem of ghost correction due to omission of odd components in the expansion becomes relevant [28]. Whereas all pole densities are positive, the harmonic ODF has negative values (Table 4). This, and the weaker ODF maximum, points to the presence of "ghosts" [29]. No ghost corrections are implemented in any Rietveld texture code.

For direct methods MAUD provides resolution ranges from 2.5° to 15°. In the case of the current configuration of HIPPO, the angular resolution of a detector panel exceeds 10° and is the limiting constraint for the angular resolution of the texture. This is to some extent governed by the binning scheme and can be changed by software in the future. In the present computation, the resolution employed for the direct methods was of 10° as displayed by the cells in the pole figure. It is very useful to see in the EWIMV pole figures no sharp variations between cells that would suggest poor data quality or major deficiencies in the analysis. The discrete appearance can easily be alleviated by smoothing (Fig. 7c). General advantages of the Rietveld method over the use of individual peak intensities are that results are less subject to systematic errors and problems with peak shape and overlaps because the solution is constrained by a physical model, allowing fewer degrees of freedom. However, the introduction of additional scaling parameters to account for uncertainties in diffraction intensities, recorded with different detectors at different times, increases the number of degrees of freedom in the refinement and leads to a loss of texture information. Highest resolution of the texture function can only be achieved if the number of scaling parameters is minimized and this includes detector sensitivity as well as precise monitor counts.

The new data for limestone establish HIPPO as an efficient instrument to measure preferred orientation. However, while quantitative texture analysis is feasible, it still requires considerable expertise from the user, both in conducting the experiment and in the analysis of data. In conclusion, it should be mentioned that texture is an important function of the HIPPO diffractometer but this instrument has much broader capabilities. A 500 ton torroidal anvil press (TAP-98) achieves $p$–$T$ conditions of 30 GPa and 2000 K for fairly large sample volumes ($< 500\,mm^3$). Vacuum furnaces with vanadium and niobium heating elements provide temperatures to 1800 K for investigations of reaction kinetics (this furnace can also be used for in situ texture studies). The automatic sample changer enables routine measurements of powders for crystallographic studies. It is anticipated that investigations of magnetic materials will be a future application of this versatile instrument.

## Acknowledgements

We are most appreciative to K. Bennett and R.B. Von Dreele, who, as members of the spectrometer development team, were instrumental for the design and construction of HIPPO. The technical staff at the Lujan Center and the University of California at Berkeley deserve credit for building this instrument, and DOE-BES, UC Office of the President, ORNL for providing financial resources. We acknowledge continued support through A. Hurd. S. Grigull helped with data processing. HRW is supported by NSF-99-02866 and IGPP-LANL, the visit of L.L. and S.G. was supported by Grant UCDRD-LANL 10014 to H.R.W.

## References

[1] K. Bennett, R.B. Von Dreele, H.-R. Wenk, in: J.A. Szpunar (Ed.), Proceedings of the 12th International Conference on Textures of Materials, NRC Research Press, Ottawa, 1999, pp. 129–134.
[2] B.N. Brockhouse, Can. J. Phys. 31 (1953) 339.
[3] D. Juul-Jensen, J.K. Kiems, Texture. Microstruct. 5 (1983) 239.
[4] H.-J. Bunge, H.-R. Wenk, J. Pannetier, Texture. Microstruct. 5 (1982) 153.
[5] H.-R. Wenk, J. Pannetier, J. Struct. Geol. 12 (1990) 177.
[6] K. Feldmann, Texture. Microstruct. 10 (1989) 309.
[7] H.-R. Wenk in: J.D. Jorgensen, A.J. Schultz (Eds.), Time-of-Flight Diffraction at Pulsed Neutron Sources, Vol. 29, Transactions of the American Crystallographic Association Buffalo, NY, 1993, pp. 95–108.
[8] H.-R. Wenk, P.J. Vergamini, A.C. Larson, Texture. Microstruct. 8–9 (1988) 443.
[9] H.-R. Wenk, A.C. Larson, P.J. Vergamini, A.J. Schultz, J. Appl. Phys. 70 (1991) 2035.
[10] K. Walther, K. Ullemeyer, J. Heinitz, M. Betzl, H.-R. Wenk, J. Appl. Crystallogr. 28 (1995) 503.
[11] K. Ullemeyer, B. Spalthoff, J. Heinitz, N.N. Isakow, A.N. Nikitin, K. Weber, Nucl. Instr. and Meth. A 412 (1998) 80.
[12] H.-R. Wenk, J. Appl. Crystallogr. 24 (1991) 920.
[13] R.B. Von Dreele, J. Appl. Crystallogr. 30 (1997) 577.
[14] H.-R. Wenk, H. Kern, W. Schaefer, G. Will, J. Struct. Geol. 6 (1984) 687.
[15] K. Bennett, H.-R. Wenk, W.B. Durham, L.A. Stern, Philos. Mag. A 76 (1997) 413.
[16] A. Mücklich, K. Hennig, J. Bouillot, S. Matthies, in: C.M. Brakman, P. Jongenburger, E.J. Mittemeijer (Eds.), Proceedings of the Seventh International Conference on Textures of Materials (ICOTOM 7), Netherlands Society of Material Science, Zwijndrecht, NL, 1984, pp. 657–662.
[17] A.C. Larson, R.B. Von Dreele, General structure analysis system (GSAS), Los Alamos National Laboratory Report LAUR 86-748, 1994.
[18] H.M. Rietveld, J. Appl. Crystallogr. 2 (1969) 65.
[19] L. Lutterotti, S. Matthies, H.-R. Wenk, A.J. Schultz, J.W. Richardson, J. Appl. Phys. 81 (1997) 594.
[20] Y. Xie, L. Lutterotti, H.-R. Wenk, J. Mater. Sci. 2003, submitted for publication.
[21] S. Matthies, G.W. Vinel, Phys. Stat. Sol. (b) 112 (1982) K111.
[22] K. Pawlik, Phys. Stat. Sol. (b) 134 (1986) 477.
[23] H.-R. Wenk, K. Pawlik, J. Pospiech, J.S. Kallend, Textures Microstruct. 22 (1994) 233.
[24] D. Chateigner, Lutterotti, L.L., T. Hansen, ILL Annual Report 97, 1998, pp. 28–29.
[25] H.-R. Wenk, S. Matthies, J. Donovan, D. Chateigner, J. Appl. Crystallogr. 31 (1997) 262.
[26] H.-J. Bunge, Texture Analysis in Materials Science—Mathematical Methods, Butterworths, London, 1982.
[27] H.-R. Wenk, S. Grigull, J. Pehl, D. Williams, LANSCE Activity Report 2002, LA-14036-PR (2003), pp. 36–39.
[28] S. Matthies, Phys. Stat. Sol. (b) 92 (1979) K135.
[29] K. Luecke, J. Pospiech, J. Jura, J. Hirsch, Z. Metallk. 77 (1986) 312.